

## Full length article

*Ab initio* prediction of vacancy energetics in HCP Al-Hf-Sc-Ti-Zr high entropy alloys and the subsystemsXi Zhang<sup>a,\*</sup>, Sergiy V. Divinski<sup>b,c</sup>, Blazej Grabowski<sup>a</sup><sup>a</sup> Institute for Materials Science, University of Stuttgart, D-70569 Stuttgart, Germany<sup>b</sup> Institute of Materials Physics, University of Münster, 48149 Münster, Germany<sup>c</sup> Samara National Research University, Moskovskoye Shosse 34, Samara 443086, Russia

## ARTICLE INFO

## Article history:

Received 19 May 2021

Revised 10 January 2022

Accepted 17 January 2022

Available online 21 January 2022

## Keywords:

*Ab initio* calculations

Vacancy energetics

High entropy alloys

Local cluster expansion

## ABSTRACT

We perform *ab initio* density-functional-theory (DFT) calculations to investigate the vacancy formation and migration energies in HCP Al-Hf-Sc-Ti-Zr high entropy alloys (HEAs) and their subsystems from binaries to quinaries. For the vacancy formation properties, we utilize the special quasi-random structure approach in conjunction with a statistical analysis, from which temperature-dependent formation Gibbs energies as well as averaged atomic environments can be extracted. We show that the temperature-dependent vacancy formation Gibbs energy due to configurational excitations has a negative configurational entropy contribution. For the vacancy migration barriers, obtained from the nudged elastic band method, we apply the local cluster expansion technique to the kinetically resolved activation barriers to explore extended vacancy migration phase spaces. The local chemical environment effect and general trends in terms of the "high entropy" effect are analyzed.

© 2022 The Author(s). Published by Elsevier Ltd on behalf of Acta Materialia Inc.  
 This is an open access article under the CC BY-NC-ND license  
 (<http://creativecommons.org/licenses/by-nc-nd/4.0/>)

## 1. Introduction

Diffusion in high entropy alloys (HEAs) has attracted significant attention in the materials science community, as a variety of key properties of industrial importance, e.g., phase stability, microstructure evolution, and mechanical properties such as creep behavior, are largely determined by atomic transport. Diffusion rates in various HEAs have been measured via the diffusion couple or the radiotracer technique [1–3]. Radiotracer measurements, for example, revealed that the initially advocated concept of "sluggish diffusion" [4] is not valid in general [5]. Diffusion parameters such as the activation energy or the prefactor could be, in principle, extracted from the measured temperature-dependent diffusion rates. This information, however, does not provide enough physical insight into the related mechanisms. In fact, tracer diffusion measurements in single crystalline CoCrFeMnNi alloys revealed strong deviations from the anticipated Arrhenius-type dependencies [6]. Such findings call for approaches that provide a thorough microscopic understanding of the observed phenomena.

Microscopically, atomic transport is mediated by defects, among which vacancies are the dominant vehicles for substitutional dif-

fusion in metallic materials. Vacancy formation and migration energies are the key quantities to understand vacancy-mediated diffusion mechanisms and the involved physics. Due to the chemical complexity, experimental measurements of vacancy properties in HEAs face challenges and thus, only a limited number of measurements has been reported [7–10]. Theoretical predictions of vacancy properties provide an alternative approach, especially since *ab initio* simulations, based on density-functional-theory (DFT), have shown great success in predicting energies of various defects, such as vacancies [11,12], stacking faults [13], or surfaces [14], in pure metals and ordered compounds. In disordered alloys challenges arise, since the formation and migration of vacancies cannot be uniquely associated with specific atomic configurations. It has been generally concluded that the chemical configuration in the vicinity of a vacancy has a strong impact on the formation energy [15–19]. Migration energies likewise depend on the local atomic arrangement [20–23]. Consequently, formation and migration energies of vacancies display a significant broadening with respect to the chemical environment. Once the distribution of individual energy states, i.e., the "density of states" (DOS) is determined, all other vacancy properties can be extracted utilizing a statistical analysis [17,24] to properly account for the finite temperature probabilities of vacancy formation.

\* Corresponding author.

E-mail address: [xi.zhang@imw.uni-stuttgart.de](mailto:xi.zhang@imw.uni-stuttgart.de) (X. Zhang).

Theoretical investigations of vacancy energetics in HEAs were so far mostly limited to systems with isotropic cubic geometry, e.g., the fcc FeCrMnNiCo-based HEAs [25–31] and the bcc VTaCrW-based HEAs [32], with one recent exception of the high-entropy metal diboride with hexagonal AlB<sub>2</sub> structure [33]. A new category of hexagonal HEAs with promising mechanical properties was reported by Rogal et al. [34] for the Al-Hf-Sc-Ti-Zr system. Recently Vaidya et al. [35] unveiled the intriguing phenomenon of ultra-fast diffusion of Co and enhanced diffusion of Zr in this HEA system and its subsystems, utilizing radiotracer measurements and *ab initio* calculations. This finding motivates further investigations of vacancy behavior in HCP HEAs, especially concerning the anisotropic behavior of vacancy migration properties.

In this work, we perform a comprehensive *ab initio* study of vacancy formation and migration properties in Al-Hf-Sc-Ti-Zr based HCP HEAs and the related subsystems. Our aim is to understand the general trends of these properties in terms of the so-called “high entropy” effect coined in the HEA community, i.e., in as far a certain materials property varies monotonously with the number of elements. In other words, we would like to reveal whether solely the number of elements or the chemical complexity plays a dominant role. We show that special care is necessary to obtain the proper statistics for vacancy concentrations in multicomponent disordered alloys at finite temperatures. In order to improve the limited sampling of the environment-dependent vacancy migration energies from nudged elastic band calculations, we additionally apply the local cluster expansion technique to coarse grain the migration density of states.

## 2. Theory

### 2.1. Vacancy thermodynamics in multicomponent concentrated alloys

It is well known that thermal vacancies are energetically not favorable at 0 K due to the broken chemical bonds in the vicinity of the vacancies. They are, however, stabilized at elevated temperatures because of the increasing configurational entropy. The equilibrium concentration of vacancies is obtained for the minimum Gibbs energy, i.e., at

$$\frac{\partial \Delta G_v}{\partial x_v} \Big|_{x_v=x_v^{\text{eq}}} = 0, \quad (1)$$

where  $\Delta G_v$  stands for the Gibbs energy change per atom due to the formation of vacancies and  $x_v$  for the vacancy concentration defined by  $x_v = n_v/N_{\text{at}}$  where  $n_v$  and  $N_{\text{at}}$  are the number of vacancies and atoms.<sup>1</sup> Both  $\Delta G_v$  and  $x_v$  are temperature and composition dependent.

[Eq. \(1\)](#) provides the starting point for a theoretical determination of the equilibrium vacancy concentration at any given temperature. A proper formulation of  $\Delta G_v$  as a function of  $x_v$  and temperature is, to this end, of critical importance. In disordered alloys, different neighborhoods around vacancies are generally associated with distinct formation energies, i.e., vacancies become “distinguishable” according to their local environment. Specifically, vacancies of type  $v_i$  are associated with a formation energy of  $\epsilon_{v_i}^f$ . As vacancy concentrations are typically low, vacancies will be on average far apart and the formation of vacancies of each type  $v_i$  can be assumed to be independent of each other. With this assumption, the total Gibbs energy change per atom due to the formation of vacancies can be then written as a sum of the Gibbs energy contributions  $\Delta g_{v_i}$  from all types of vacancies, i.e.,

$$\Delta G_v = \sum_i \Delta g_{v_i} = \sum_i (x_{v_i} \epsilon_{v_i}^f - T \Delta s_{v_i}), \quad (2)$$

<sup>1</sup> As the vacancy concentration is defined here by the atomic fraction, the concentration of each component and of the vacancies do not add up to unity.

where  $x_{v_i}$  is the vacancy concentration of type  $v_i$  and  $\Delta s_{v_i}$  the corresponding configurational entropy per atom. The equilibrium concentration of vacancy of type  $v_i$  can then be obtained by minimizing the total Gibbs energy change with respect to the concentration of type  $v_i$ , i.e.,

$$\frac{\partial \Delta G_v}{\partial x_{v_i}} \Big|_{x_{v_i}=x_{v_i}^{\text{eq}}} = 0. \quad (3)$$

Generally, the vacancy concentration  $x_{v_i}$  of type  $v_i$  is given by a product of the concentration of all possible vacancy states with energy  $\epsilon_{v_i}^f$  and the probability of activating these states,  $p_{v_i}$ , at finite temperatures. The concentrations can be obtained from the density of vacancy formation states  $D(\epsilon^f)$ , which we will abbreviate as VF-DOS and which describes the number of vacancy states with a formation energy within a small interval around  $\epsilon^f$ . The normalized VF-DOS, i.e.,  $\tilde{D}(\epsilon_{v_i}^f) = D(\epsilon_{v_i}^f) / \sum_i D(\epsilon_{v_i}^f)$  provides the fraction of all possible vacancy states with energy  $\epsilon_{v_i}^f$ . The probabilities  $p_{v_i}$  are related to the formation energies  $\epsilon_{v_i}^f$  since a higher vacancy formation energy corresponds to a lower probability of being activated. The vacancy concentration  $x_{v_i}$  of type  $v_i$  then reads,

$$x_{v_i} = \tilde{D}(\epsilon_{v_i}^f) p_{v_i}, \quad (4)$$

where  $p_{v_i}$  can be solved after determination of the configurational entropy.

The expression for the configurational entropy should be derived with special care, i.e., the reference state should be properly defined. Physically, the formation of vacancies preserves the chemical configuration of the alloy. For low vacancy concentrations, the configurational entropy contribution from vacancies of type  $v_i$  can be represented by an ideal mixing entropy via the Boltzmann equation,

$$\Delta s_{v_i} = \frac{1}{N_{\text{at}}} k_B \ln W = \frac{1}{N_{\text{at}}} k_B \ln \frac{(N_{\text{at}} \tilde{D}_{v_i})!}{(N_{\text{at}} \tilde{D}_{v_i} - N_{\text{at}} \tilde{D}_{v_i} p_{v_i})! (N_{\text{at}} \tilde{D}_{v_i} p_{v_i})!}, \quad (5)$$

where  $W$  is the total number of microstates and  $k_B$  the Boltzmann constant. The energy-dependence of the VF-DOS has been replaced by a subscript  $v_i$  for notational brevity. Further simplification of [Eq. \(5\)](#) with Stirling's approximation yields

$$\Delta s_{v_i} = -k_B \tilde{D}(\epsilon_{v_i}^f) [p_{v_i} \ln(p_{v_i}) + (1 - p_{v_i}) \ln(1 - p_{v_i})]. \quad (6)$$

Note that [Eq. \(6\)](#) is conceptually different from what has been derived in previous studies [24,33], where the derivative in [Eq. \(1\)](#) was taken from the ideal entropy described as the sum of the logarithmic term of each element  $j$  and the vacancy, i.e.,  $\Delta S = -k_B \sum_j y_j \ln y_j - k_B y_v \ln y_v$ ,  $j = 1, 2, \dots, N$ , for an  $N$ -component alloy and with the condition that  $\sum_j y_j + y_v = 1$  indicating that  $y_j$  defines the site fraction of element  $j$  and  $y_v = n_v/(N_{\text{at}} + n_v)$ ; further, the composition of the alloy was assumed to be preserved. However, a description according to such an equation does not preserve the chemical configuration of the alloy during the formation of vacancies, because of the incorrect implicit assumption that the elements can reorganize when vacancies are created. In consequence, the vacancy concentration scales with a factor of  $1/N$  for equiatomic  $N$ -component alloys, which is physically incorrect. This has been also pointed out in a recent comment where a correction for the derivation in Ref. [24] was proposed [36] based on the assumption that the system exhibits a uniform vacancy formation energy. The configurational entropy described by [Eq. \(6\)](#) does not rely on such an assumption but applies in general to systems with multiple vacancy formation energies.

With the total Gibbs energy per atom obtained by substituting the proper description of the entropy from [Eq. \(6\)](#) together with [Eq. \(4\)](#) into [Eq. \(2\)](#), the concentration of vacancies of type  $v_i$  can be calculated by minimizing [Eq. \(3\)](#) with the assumption that  $x_{v_i}$

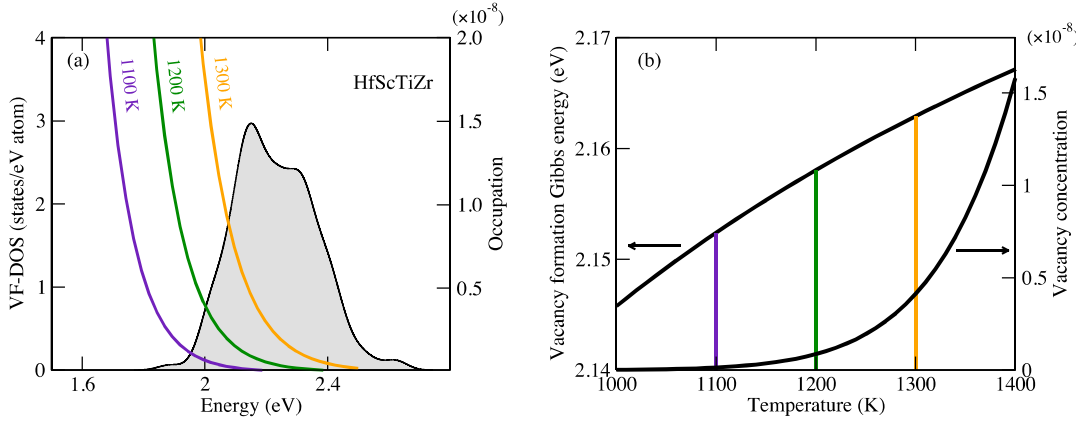


**Fig. 1.** Illustration of the temperature-dependent excitations of vacancy states with different local environments for HfScTiZr. The colored lines in (a) show the occupation curves calculated from the Boltzmann factor for three different temperatures. The corresponding vacancy concentrations and formation Gibbs energies are indicated in (b) by the respective colors.

is much smaller than  $\tilde{D}(\epsilon_{v_i}^f)$ , i.e.,  $p_{v_i} \ll 1$ , which gives

$$x_{v_i} = \tilde{D}(\epsilon_{v_i}^f) \exp(-\beta \epsilon_{v_i}^f), \quad (7)$$

with  $\beta = 1/k_B T$ . A comparison of Eq. (7) and Eq. (4) gives the expression for  $p_{v_i}$ ,

$$p_{v_i} = \exp(-\beta \epsilon_{v_i}^f), \quad (8)$$

viz., the Boltzmann function for describing thermal excitations, which is analogous to the general expression of the equilibrium vacancy concentration in unary systems. The temperature-dependent total equilibrium vacancy concentration is then obtained from the sum of all possible types, i.e.,

$$x_v^{\text{eq}}(T) = \sum_i x_{v_i} = \sum_i \tilde{D}(\epsilon_{v_i}^f) \exp(-\beta \epsilon_{v_i}^f). \quad (9)$$

From Eq. (9), it is apparent that in multicomponent disordered alloys the vacancy concentration does not necessarily follow an Arrhenius relation, because each exponential term in the summation is different. Eq. (9) can be physically understood by considering the temperature dependence of configurational excitations of vacancy states, as illustrated in Fig. 1(a). As the temperature increases, e.g., from 1100 K to 1300 K, the occupation curve calculated by the Boltzmann factor in Eq. (9) shifts towards higher energy states. This means that at low temperatures only vacancies with low formation energies get “excited” while at high temperatures higher energy states may be excited as well. At a fixed temperature, the total vacancy concentration is obtained by the integration of the VF-DOS weighted by the occupation number. There must be then a negative excess configurational entropy associated with the formation energy. The resulting effective formation energy is better represented as a temperature-dependent “Gibbs energy” in terms of configurational excitations. By fitting the temperature-dependent total vacancy concentration to the Arrhenius ansatz, the effective vacancy formation Gibbs energy reads

$$\tilde{G}_v^f(T) = -k_B T \ln x_v^{\text{eq}}(T). \quad (10)$$

Based on the exemplary VF-DOS in Fig. 1(a), the resulting vacancy concentration and  $\tilde{G}_v^f(T)$  are shown in Fig. 1(b). As expected,  $\tilde{G}_v^f$  increases with increasing temperature due to the above discussed configurational excitation mechanism. Utilizing the thermodynamic relation

$$\tilde{S}_v^f(T) = -\frac{\partial \tilde{G}_v^f(T)}{\partial T}, \quad (11)$$

the temperature-dependent effective vacancy formation entropy  $\tilde{S}_v^f(T)$  can be obtained. To facilitate the standard Arrhenius analysis

for diffusion, for a certain temperature range of interest from  $T_1$  to  $T_2$  that is not too large, the temperature-independent effective vacancy formation entropy  $\tilde{S}_v^f$  and enthalpy  $\tilde{H}_v^f$  can be extracted via,

$$\tilde{S}_v^f = -[\tilde{G}_v^f(T_1) - \tilde{G}_v^f(T_2)]/(T_1 - T_2) \quad (12)$$

and

$$\tilde{H}_v^f = \tilde{G}_v^f(T_1) + T_1 \tilde{S}_v^f. \quad (13)$$

Another vacancy property of interest in disordered alloys is the average concentration of the vacancy neighborhood which can be experimentally determined via positron annihilation spectroscopy coupled with the coincidence Doppler broadening technique [10]. In an  $N$ -component alloy, the average concentration of a species  $s$  ( $s = 1, 2, \dots, N$ ) in the nearest neighbor shell of vacancies depends also on temperature, which reads

$$\bar{x}_v^{s,\text{shell}}(T) = \frac{1}{Z} \frac{1}{x_v^{\text{eq}}(T)} \sum_{i,j} x_{v_i}(T) w_j n_{j,v_i}^{s,\text{shell}}, \quad (14)$$

where  $n_{j,v_i}^{s,\text{shell}}$  indicates the number of elements of type  $s$  in one specific nearest neighbor shell  $j$  of vacancy type  $v_i$  and  $w_j$  is the corresponding concentration weight in  $\tilde{D}(\epsilon_{v_i}^f)$  and  $Z$  the coordination number. For HCP structures, the number of the nearest neighbor atoms is 12 when the  $c/a$  ratio is ideal. For alloys with a non-ideal  $c/a$ , i.e., for all investigated alloys in this work, atoms in the 1st (6 atoms) and 2nd (6 atoms) shells are all included.

## 2.2. Local cluster expansion for vacancy migration barriers

Unlike in pure metals, vacancies in multicomponent disordered alloys experience a rugged potential energy surface where both, the local minima and the saddle points have wide energy distributions. It was remarked in a previous study [22] that, even in binary alloys, the vacancy migration barriers can vary by as much as a factor of 3. It can be thus expected that in multicomponent alloys such as HEAs the vacancy migration barrier distribution is yet more complex. More importantly, such nonuniform barriers may result in a strongly correlated vacancy migration behavior that deviates from a random walk and thus results in different diffusion kinetics. Previous kinetic Monte Carlo simulations have indeed shown that specific barrier distributions may even kinetically drive the formation of ordered precipitates in phase separation alloys [23]. It is then of critical importance, before any analysis of the diffusion kinetics, to know the vacancy migration barrier distribution, i.e., the density of vacancy migration states  $D(\epsilon^m)$  (which we will abbreviate as VM-DOS in the following).

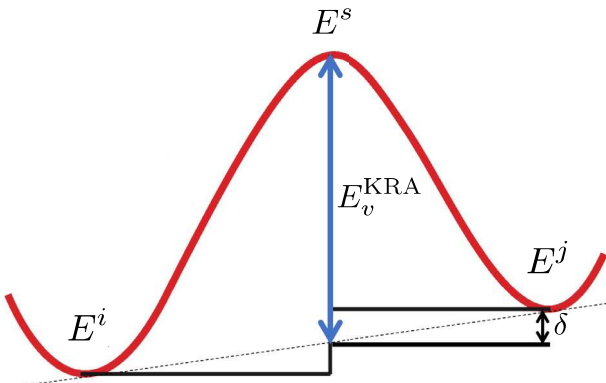


**Fig. 2.** Schematic illustration of the KRA barriers  $E_v^KRA$  given by Eq. (15).

Nowadays, *ab initio* predictions of vacancy migration barriers generally rely on DFT based nudged elastic band (NEB) calculations. This method, however, is computationally demanding if one aims at a reasonably well converged VM-DOS in multicomponent alloys. In order to efficiently probe an extended vacancy migration phase space, we apply here the local cluster expansion (LCE) technique as described in Ref. [23] to parametrize the environment-dependent kinetically resolved activation (KRA) migration barriers [20],

$$E_v^KRA = E^s - (E^i + E^j)/2, \quad (15)$$

where superscripts  $s$ ,  $i$ , and  $j$  refer to configurations of the saddle point and the two end points (see Fig. 2). An advantage of using the KRA barriers is that they describe direction independent migration energies which facilitates the LCE parametrization. The actual direction-dependent migration barriers, i.e.,  $E^{i \rightarrow j}$  and  $E^{j \rightarrow i}$ , can be recovered using  $E_v^KRA \pm \delta$ , where  $\delta = |E^i - E^j|/2$  (see Fig. 2). To properly define the cluster geometry as conventional CE does, special treatment is necessary because putting the diffusing atom at the saddle position violates the fixed lattice approximation. We employ the formalism of Refs. [18,23] and introduce  $N$  types of new “pseudoatomic pairs (PP)” to describe the transition states of an  $N$ -component alloy (as schematically shown in Fig. 3). This procedure results in  $N$  “( $N+1$ )-component” LCEs to be fitted. More specifically, e.g., in an ABCDE 5-component HEA, for the diffusing atom of species S ( $S = A, B, C, D$ , and  $E$ ) at the transition state, the “S-Vac pair” is replaced by a new “X-X” pair ( $X = F, G, H, I$ , and  $J$ ), yielding an ABCDEX 6-component LCE. For each LCE, all effective cluster interactions (ECIs) associated with one arbitrarily selected alloying element (ASAE) can be ignored due to the sum rule [22]. The corresponding KRA barriers are expanded as

$$E_v^{\text{mkra}} = J_\beta + \sum_{\alpha} n_{\beta \cup \alpha} J_{\beta \cup \alpha}, \quad (16)$$

where  $J_\beta$  is the ECI of the jumping atom purely surrounded by the ASAE,  $\beta$  represents the PP,  $\alpha$  represents a cluster decoration corresponding to the empty cluster, or a point cluster, etc. but not part of the PP.  $n_{\beta \cup \alpha}$  and  $J_{\beta \cup \alpha}$  refer to the number of cluster decorations of type  $\beta \cup \alpha$  and the corresponding ECI. Note that, when determining which cluster decorations should be included in the LCE, the PP should be always included as a subcluster of the selected ones for geometric distinction [22].

Another important technical issue of the LCE is that the KRA barriers predicted via Eq. (16) are not necessarily positive. This is undesired because diffusion barriers are generally positive. To avoid unphysical predictions, an additional restriction should be added to the ECI selection procedure such that the following crite-

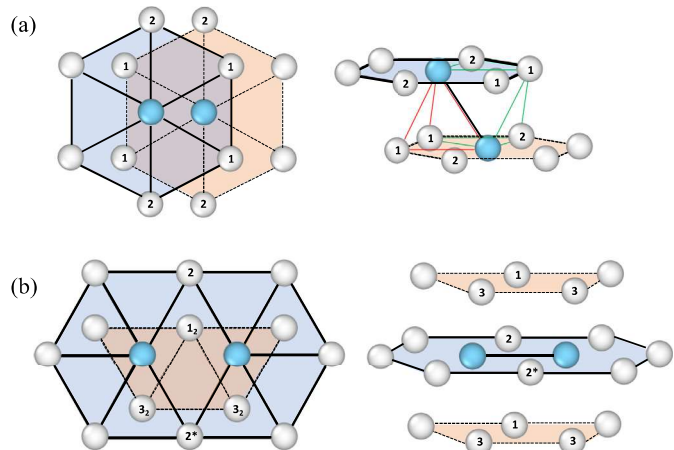


**Fig. 3.** Schematic illustration the anisotropy of the vacancy migration in hcp alloys: (a) diffusion out of the basal plane and (b) diffusion within the basal plane. For each subfigure, the left side shows the view projected to the hcp basal plane. Blue atoms represent the “pseudoatomic pair (PP)” introduced in the LCE by replacing the pair of the jumping atom and its neighbor vacancy. Numbers labeled on the surrounding atoms of the PP indicate the sequence of the distance to the center of the PP. The asterisk attached to the number indicates that the distance is the same but atoms are geometrically distinct. The tetrahedron (red lines) and the octahedron (green lines) shown in (a) represent the maximal clusters in the cluster pool for the LCEs. (For interpretation of the references to colour in this figure legend, the reader is referred to the web version of this article.)

tion is satisfied

$$J_\beta + \frac{1}{2} \sum_{\alpha'} n_{\beta \cup \alpha}^{\max} (J_{\beta \cup \alpha} - |J_{\beta \cup \alpha}|) > 0, \quad (17)$$

where  $n_{\beta \cup \alpha}^{\max}$  is the maximum value of the  $n_{\beta \cup \alpha}$  counter and  $\alpha'$  in the sum indicates that the empty cluster is excluded. Practically, an alternative efficient screening approach, as implemented in this work, is to first generate a large number of random migration configurations. Generally, these local migration configurations can be randomly selected from multiple random structures at the target composition. It is then required in the selection procedure that the predicted KRA barriers within the configuration pool are all higher than some preset positive value.

### 3. Computational details

To sample the VF-DOS for all investigated alloys, i.e., HfZr, HfTiZr, HfScTiZr, Al<sub>5</sub>Hf<sub>25</sub>Sc<sub>20</sub>Ti<sub>25</sub>Zr<sub>25</sub> (HEA\_5Al), and Al<sub>15</sub>Hf<sub>25</sub>Sc<sub>10</sub>Ti<sub>25</sub>Zr<sub>25</sub> (HEA\_15Al), *ab initio* DFT calculations were performed utilizing the supercell approach. Previous *ab initio* calculations for vacancies [11] and other point defects [35] indicate that supercells of around 100 atoms suffice to minimize finite size effects. In order to acquire sufficient statistics, for each investigated alloy, we used two special quasirandom structures [37] (SQS) with 96 atoms for each ( $4 \times 4 \times 3$  expansion of the HCP primitive cell) to mimic the single-phase random solid solutions. We have tested the resulting vacancy concentrations and effective vacancy formation Gibbs energies based on 96 samples and 192 samples (see Figs. S2 and S3 in Supplemental Material). The changes are very minor especially at the temperature range where diffusion is experimentally measured. Note in particular that the difference between 96 and 192 samples cannot be taken as an error estimate because the results for 192 samples must be significantly better converged than for 96 samples. The true error will be much smaller. Thus, we do not expect further changes with increasing the number of samples. The subsequent analysis and discussions are based on the results of 192 samples.

Potentials based on the projector augmented wave method [38], as implemented in VASP [39,40], were used in conjunction with the generalized gradient approximation (GGA) in the parametrization of Perdew-Burke-Ernzerhof (PBE) [41]. The potentials included semicore  $s$  ( $p$ ) electrons as valence electrons for Sc and Zr (Hf and Ti). The plane wave cutoff was set to 268 eV for all calculations. The Methfessel-Paxton scheme [42] of order 1 with a smearing value of 0.1 eV was used to treat partial occupancies. Integration in reciprocal space was based on a  $\Gamma$ -centered Monkhorst-Pack grid [43] with the number of  $k$ -points determined by  $N_{\text{atom}} \times N_{\text{k-point}} \approx 10000$ . Each vacancy-free SQS supercell and each pure metal supercell were first fully relaxed with respect to all degrees of freedom using the conjugate-gradient algorithm. The total energy was then obtained from an additional static calculation using the same parameters to remove the impact of Pulay stresses introduced by the previous volume relaxation. For each relaxed SQS structure, a vacancy was created once at every site, giving rise to 96 different supercells, each with a single vacancy. With two SQSs for each alloy, we obtained  $96 \times 2 \times 5 + 5 = 965$  supercells with a single vacancy. Total energies of all these vacancy supercells were then obtained by performing ionic relaxations only (cell shape and volume fixed). The relaxation was stopped when the total energy converged to 0.01 eV/cell. The formation energies of all sampled vacancy states, i.e., vacancies with a different local chemical environment, were extracted via

$$\epsilon_{v_i}^f = E(\text{SQS} + v_i) - E(\text{SQS}) + \mu_i, \quad (18)$$

with  $\mu_i$  being the chemical potential of the removed atom of type  $i$ . The chemical potential defined here refers to the derivative of the enthalpy (0 K) at zero pressure instead of the Gibbs energy as a function of the alloy composition as we neglect all temperature-dependent contributions such as thermal effects as well as the alloy's configurational entropy contribution. Generally, the chemical potential of an element in concentrated alloys deviates from the value in the respective pure metal, depending on the alloy's mixing behavior. We therefore explicitly calculated the chemical potential of each species in all investigated alloys following the concept of the Widom-type substitution [44]. The key strategy is to numerically estimate the derivative of the mixing enthalpy at a fixed composition with finite difference approximations. More specifically, when one atom of type  $i$  in one SQS supercell is replaced by type  $j$ , creating a finite (minimal) difference in the composition, the resulting energy difference represents the chemical potential difference between  $i$  and  $j$

$$\mu_j - \mu_i = \langle \Delta E_{i \rightarrow j} \rangle, \quad (19)$$

where the angle brackets indicate an average over several different replacements. Note that Eq. (19) differs from the original formula in Ref. [44] where the derivations are based on free energies. In fact, the present approach corresponds to the Widom substitution strategy at 0 K. We show in Fig. S1 of the Supplemental Material that, for all the investigated alloys, 10 different replacements are sufficient for converging the chemical potentials. In an  $N$ -component system,  $N - 1$  substitutions among elements, e.g., A  $\rightarrow$  B and A  $\rightarrow$  C in an A-B-C ternary alloy, are required for obtaining  $N - 1$  independent equations. Together with the following general relation

$$E(\text{SQS}) = \sum_i n_i \mu_i, \quad (20)$$

where  $n_i$  is the number of atoms of species  $i$ , the chemical potential of species  $i$  can be extracted. For all structures related to the chemical potential calculations, the DFT ionic relaxations are performed at zero pressure, i.e., the volume and the cell shape are fully relaxed.

The vacancy migration energies were calculated using the climbing image nudged elastic band (CI-NEB) method [45,46]. For

HCP alloys, it is well known that diffusion is anisotropic due to the fact that vacancy migration within the basal plane is geometrically inequivalent to that along the  $c$  axis. The migration energies for these two scenarios should be thus calculated separately. Since the migration energy of a vacancy depends also on the type of atom it exchanges the position with, for each type of atom in each investigated alloy, we selected 15 individual migration paths along each diffusion direction to perform the NEB calculations. For each individual migration path, with two relaxed vacancy structures as the initial and final states, five linearly-interpolated intermediate images (structures) were generated for finding the minimum energy pathway. The spring constant between the images was set to  $-5 \text{ eV}/\text{\AA}^2$ . The NEB ionic relaxation with the quasi-Newton algorithm was stopped when all the forces were smaller than  $0.05 \text{ eV}/\text{\AA}$ . The total energies of all intermediate images, together with the two end points, were fitted to a force-based cubic spline interpolation using the tangential forces as input to accurately locate the saddle point, as implemented in the VTST-scripts [46]. The corresponding KRA barrier of each migration path was then calculated by Eq. (15).

For all investigated alloys, we expanded the KRA barriers for each type of vacancy migration by an LCE. To obtain good LCEs which can reproduce the DFT KRA barriers, we defined first a cluster pool including a four-body tetrahedron and a six-body octahedron as well as their subclusters (14 clusters in total). Since each site of a cluster can be decorated with one of the alloying species, e.g., a pair cluster can be A-A or A-B or B-B for a binary, all different cluster decorations form the basis pool (correlation functions pool) from which the ones including the PP are only allowed to be selected. We applied the Aufbau algorithm discussed in Ref. [22] for the basis selection procedure. All the LCEs were optimized to reproduce the DFT KRA barriers with an error below 0.05 eV. The resulting root-mean-square error (RMSE) of fitting and the leave-one-out cross validation (LOOCV) score of all LCEs on average are 0.013 eV and 0.03 eV, respectively.

## 4. Results and discussion

### 4.1. Vacancy formation energies at zero Kelvin

The chemical potentials of each alloying element in the investigated alloys computed according to Eqs. (19) and (20) are shown in Fig. 4. Deviations of the chemical potential in the alloys with respect to the pure metals are generally within a range of  $\pm 0.1$  eV, except for Al where a value of  $-0.7$  eV is reached. Positive deviations, as for Ti and Sc, indicate that addition of these elements is unfavorable and will increase the system's mixing enthalpy. Vice versa, a negative chemical potential as observed for Al indicates a favorable decrease of the mixing enthalpy. These results are consistent with the calculated mixing enthalpies of the alloys listed in Table 1, e.g., an increase of the Al content results in a significant decrease of the mixing enthalpy (cf.  $H_{\text{mix}}$  for HEA\_5Al and HEA\_15Al). The large negative chemical potential of Al indicates that the addition of Al may lead to the formation of ordered phases, as shown in Ref. [34]. For the binary HfZr, the chemical potentials in the alloy are the same as in the pure metals suggesting an ideal mixing behavior of the HfZr alloy ( $H_{\text{mix}} = 0$ ), which is consistent with a previous *ab initio* study [47].

With the calculated chemical potentials and the total energies of structures with and without vacancy, vacancy formation energies for various local chemical environments were computed using Eq. (18). The resulting VF-DOS' are shown in Fig. 5(b)-(f), with the pure metals' formation energies given in Fig. 5(a) for comparison. To obtain smooth VF-DOS', the discrete set of computed formation

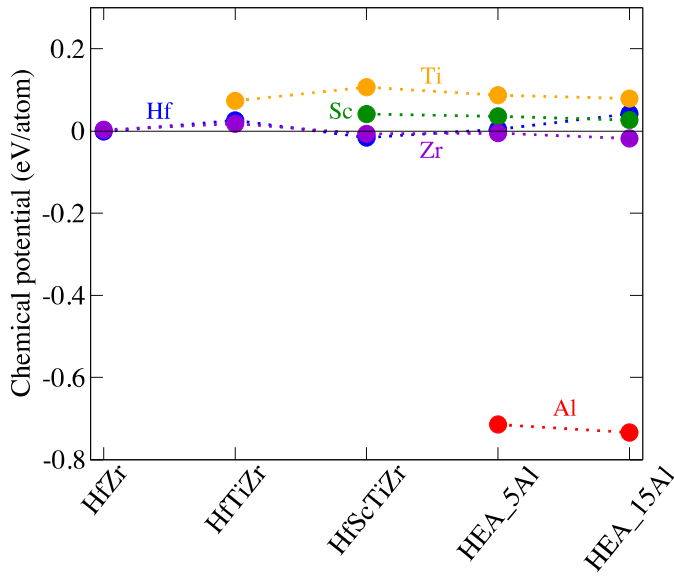


**Fig. 4.** Chemical potentials (referenced with respect to the total energy (eV/atom) of the corresponding pure metals) for all investigated alloys considered in this work.

energies was replaced by a sum of Gaussian functions,

$$D(\epsilon) = \frac{1}{\sigma \sqrt{\pi}} \sum_i \exp \left( -\frac{(\epsilon - \epsilon_i)^2}{\sigma^2} \right), \quad (21)$$

with the smearing parameter  $\sigma$  set to 0.05 eV. The mean value of the sampled energy states for each alloy is listed in the column of  $\bar{\epsilon}^f$  in Table 1 and marked for each VF-DOS by a vertical black line.

The VF-DOS' exhibit a large broadening and thus reveal a strong dependence of the formation energies on the local chemical environment. An increase of the broadening can be observed along with an increase of the number of the elements in the alloys ("high entropy" effect). When moving from the HfZr binary to the HEAs, the broadening increases by more than a factor of two. The strong broadening in the HEA VF-DOS' can be attributed to a large extent to the addition of Al which modifies the bonding energetics strongly as already revealed by the chemical potential analysis.

The mean formation energy (solid vertical lines in Fig. 5), however, does not show any monotonous trend with the number of elements. Moving from the binary to the ternary by adding Ti, a decrease of  $-0.11$  eV is observed while further addition of Sc to the ternary significantly increases the mean formation energy by  $+0.23$  eV. Adding Al decreases again the mean formation energy by  $-0.11$  eV from the quaternary system to the HEA\_5Al and once again by  $-0.11$  eV when moving to the HEA\_15Al. Unlike the previously reported results for the Cantor alloy, where vacancy formation energies in HEAs were shown to be evidently higher than in the subsystems (see Table 3 of Ref. [31]), we observe a decrease of the mean formation energies in the investigated HCP HEAs compared to the subsystems. This suggests that the type of element instead of the number of species in the alloys plays the critical role in the process of vacancy formation. This statement is further supported by the shift in the mean energies for the two quinary HEAs with the same number of elements. Here, the variation of the composition, i.e., changing the Al-Sc ratio, must be responsible for the modification of the VF-DOS.

We further examined the so-called "Vegard's law", i.e., a composition-weighted linear interpolation of the formation energies of the pure metals. We list the predicted values in the column labelled  $E_v^{\text{Veg}}$  in Table 1 and mark them by vertical dashed lines in Fig. 5. Except for the binary HfZr, the predictions of Vegard's law

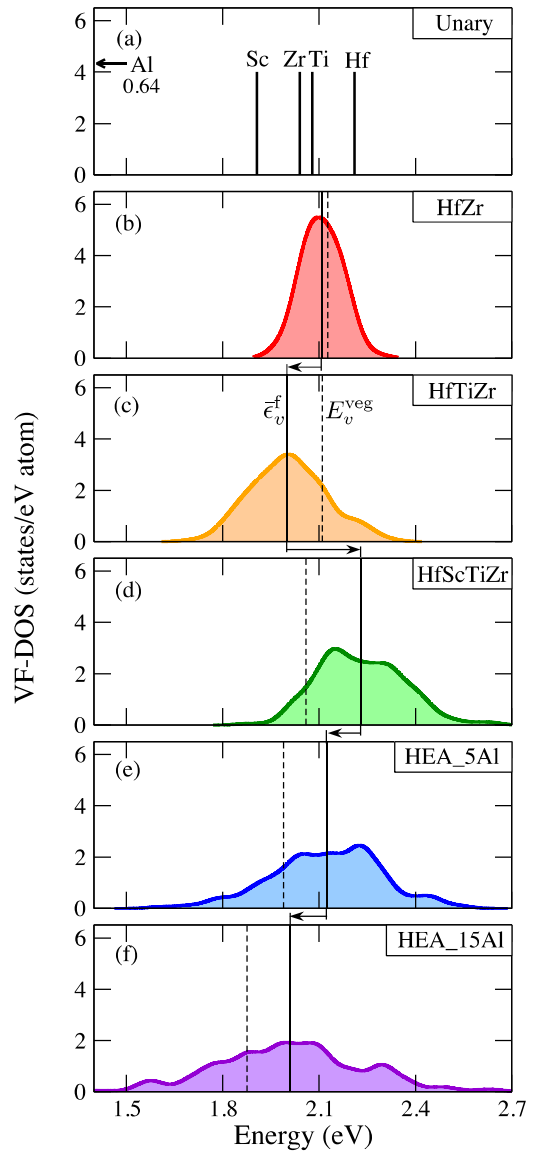


**Fig. 5.** Calculated densities of vacancy formation states (VF-DOS) for the investigated alloys. The formation energies of the pure metals are plotted in (a) for comparison. The mean value of each VF-DOS and the value predicted by Vegard's law are marked by the vertical solid and dashed line, respectively. The arrows between consecutive subfigures indicate the shift of the mean value.

generally exhibit significant deviations from the mean values. In the following section, we will show that at elevated temperatures neither the prediction from Vegard's law nor the mean value of the VF-DOS are representative of the effective vacancy formation energy due to the thermal excitations of various chemical environments.

To analyze the impact of the local chemical environment on the vacancy formation energy, we plot in Fig. 6 the calculated vacancy formation energies as a function of the number of the alloying elements in the 1st and 2nd neighbor shells of the vacancy. Each row in Fig. 6 is plotted for one investigated alloy and each column for one constituent element. The connected colored solid circles highlight the mean values of the respective local vacancy neighborhood and the general trend.

A nice and clear correlation, almost without any scatter, can be observed for the HfZr binary. This result is consistent with the observation made already above that Vegard's law applies in this system. We can now, in particular, clarify that the broadening ob-

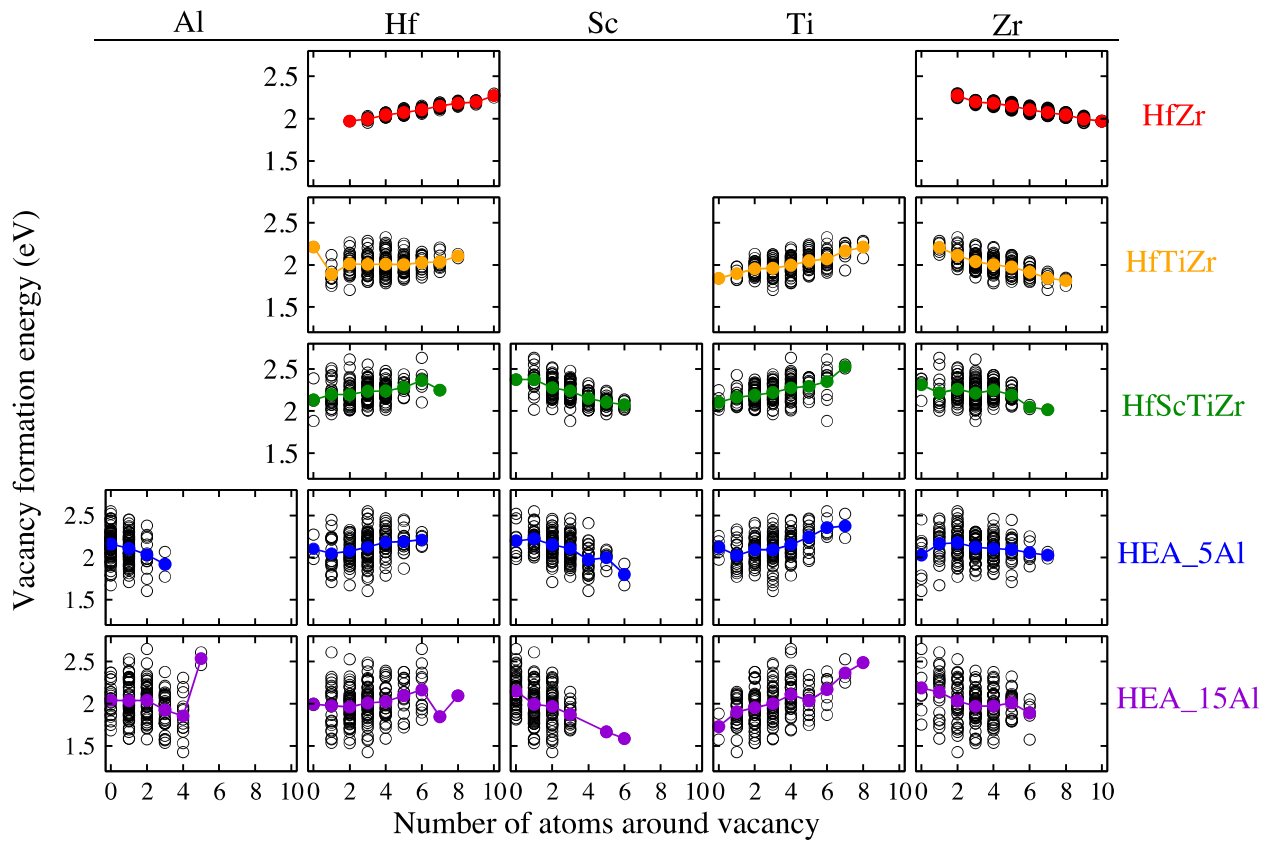


**Fig. 6.** Environment-dependent vacancy formation energies for all investigated alloys. Each column shows the energy distribution as a function of the number of one of the alloying elements in the vacancy neighborhood.

served in Fig. 5(b) is mostly due to the linear change of the vacancy formation energy with the concentration. The particular local chemical environment is less important.

The situation changes when moving to the higher order systems. The scatter in the chemically resolved vacancy formation energies (black open circles) becomes significant. This means that the specific chemical configuration in the vacancy neighborhood has a strong impact on the formation energy. Likewise atoms with larger distances to the vacancy (beyond 1st and 2nd) may have an impact as well. We note that a similarly strong impact of alloying elements was found in Ref. [35] on chemically resolved interstitial formation energies of Co.

Despite the scatter observed in Fig. 6 for the ternary and higher order systems, it is possible to extract chemical trends by analyzing the mean values of the chemically resolved formation energies. In particular, we observe that vacancies favor an environment which contains more Al, Sc, and Zr atoms, i.e., the mean formation energies decrease when the number of these elements increases in the vacancy neighborhood. In contrast, for Hf- and Ti-rich neighborhoods vacancy formation is typically not favorable. For Hf, this tendency becomes less evident for the two quinary HEAs. These general trends can be partly attributed to the low (high) vacancy formation energies of the pure Al and Sc (Ti) metals. Moreover, the feature that vacancies favor a certain type of element suggests an increasing mobility of that type of atom in the vacancy-mediated diffusion process as atomic movement can only occur when there is a vacancy nearby.

#### 4.2. Properties of vacancy formation at finite temperatures

Utilizing the VF-DOS' (Fig. 5), the total equilibrium vacancy concentration for each alloy was computed using Eq. (9) and is dis-

played in Fig. 7 versus the inverse absolute temperature (a) and the inverse homologous temperature (b). The logarithmic plot of the vacancy concentration as a function of the inverse temperature reveals deviations from the Arrhenius dependence, i.e., a curvature in the lines can be observed. The non-Arrhenius behavior originates from the fact that, in contrast to the case of a uniform formation energy in pure metals, each local vacancy neighborhood has its own vacancy formation energy in an alloy. At low temperatures only those vacancy neighborhoods with low formation energies provide vacancies, while at high temperatures sites with high formation energies may be excited as well, as discussed in Section 2.1. The non-Arrhenius feature is more pronounced when the VF-DOS has a wider distribution, cf. the binary vs. the higher order systems in Fig. 5.

It should be emphasized that the magnitude of the vacancy concentration Fig. 7(a) and (b) does not follow any clear systematic dependence with the number of components in the alloys, at least when the whole temperature range is considered. This clarifies that the individual, local vacancy formation energies play the dominant role in determining vacancy concentrations rather than the number of components. For the (inverse) absolute temperature plot Fig. 7(a), at low temperatures, the concentrations of the different alloys are spread by 4 orders of magnitude, with HEA\_15Al (HfZr and HfScTiZr) being the highest (lowest). The vacancy concentration of the HfTiZr ternary becomes the second highest among the investigated alloys in the homologous temperature plot Fig. 7(b) due to a higher melting point as compared to the HEA\_5Al alloy. At high temperatures, the vacancy concentrations of all alloys come closer together, with remaining differences below one order of magnitude. The relative magnitude is roughly inversely correlated with the sequence of the mean values of the VF-DOS' (cf. the inset of Fig. 7 and column  $\bar{\epsilon}_v^f$  in Table 1): HfTiZr and HEA\_15Al are

**Table 1**

Calculated thermodynamic quantities of vacancy formation for all investigated alloys.  $H_{\text{mix}}$ : mixing enthalpy of the alloy;  $T_m$ : melting point;  $\tilde{H}_v^f$  and  $\tilde{S}_v^f$ : the temperature-independent effective enthalpy and entropy of vacancy formation;  $\bar{\epsilon}_v^f$ : mean value of the sampled VF-DOS;  $E_v^{\text{Veg}}$ : vacancy formation energy predicted by Vegard's law.

| Alloy    | $H_{\text{mix}}$<br>(meV/at) | $T_m$<br>(K)      | $\tilde{H}_v^f$ (eV) |                   | $\tilde{S}_v^f$ ( $k_B$ ) |                   | $\bar{\epsilon}_v^f$<br>(eV) | $E_v^{\text{Veg}}$<br>(eV) |
|----------|------------------------------|-------------------|----------------------|-------------------|---------------------------|-------------------|------------------------------|----------------------------|
|          |                              |                   | $T_{\text{low}}$     | $T_{\text{high}}$ | $T_{\text{low}}$          | $T_{\text{high}}$ |                              |                            |
| HfZr     | 0                            | 2317 <sup>a</sup> | 2.06                 | 2.08              | -0.31                     | -0.11             | 2.11                         | 2.13                       |
| HfTiZr   | 39                           | 2192 <sup>a</sup> | 1.85                 | 1.91              | -0.95                     | -0.36             | 2.00                         | 2.11                       |
| HfScTiZr | 31                           | 2038 <sup>b</sup> | 2.04                 | 2.11              | -1.11                     | -0.42             | 2.23                         | 2.06                       |
| HEA_5Al  | -9                           | 2053 <sup>a</sup> | 1.72                 | 1.87              | -2.40                     | -1.01             | 2.12                         | 1.99                       |
| HEA_15Al | -78                          | 1965 <sup>a</sup> | 1.54                 | 1.68              | -2.48                     | -1.21             | 2.01                         | 1.88                       |

<sup>a</sup>taken from Ref. [35]. <sup>b</sup>calculated from Thermocalc SSOL6 database.

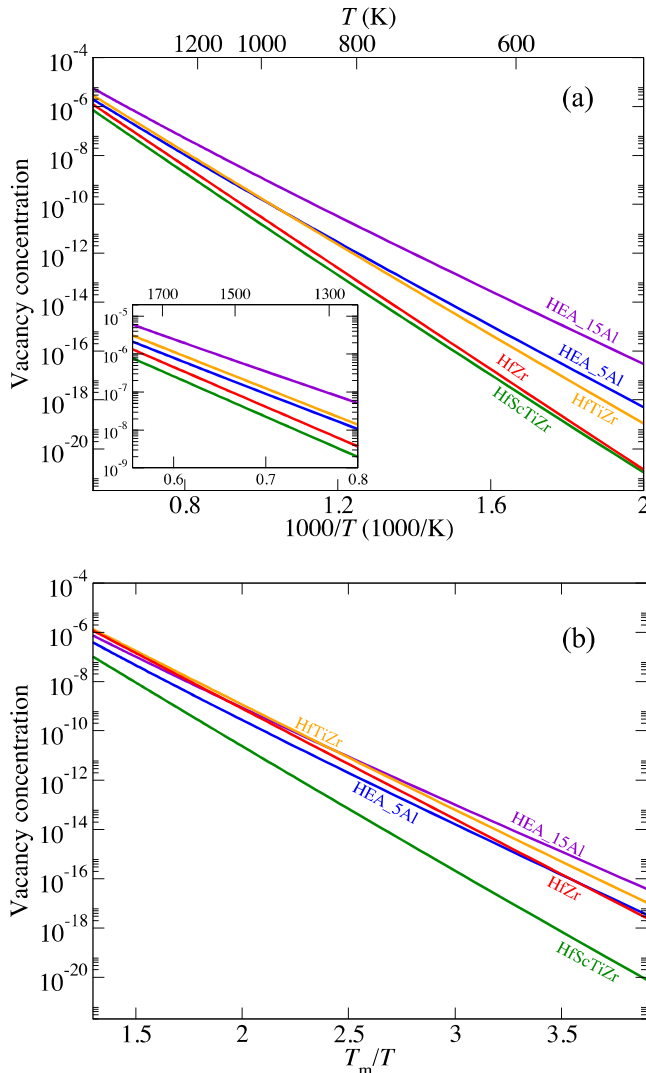


**Fig. 7.** Calculated vacancy concentrations as a function of (a) the inverse absolute temperature and (b) the inverse homologous temperature for all investigated alloys. The melting points are listed in Table 1.

the highest while the 4-component alloy is the lowest, indicating an intersection point of the ternary HfTiZr and HEA\_5Al at some intermediate temperature. The similar vacancy concentrations at high temperatures can be understood from the fact that different contributions to the total vacancy concentration from various local vacancy neighborhoods get smeared out as all kinds of vacancies start to be equally excited. Such a smearing effect is closely related

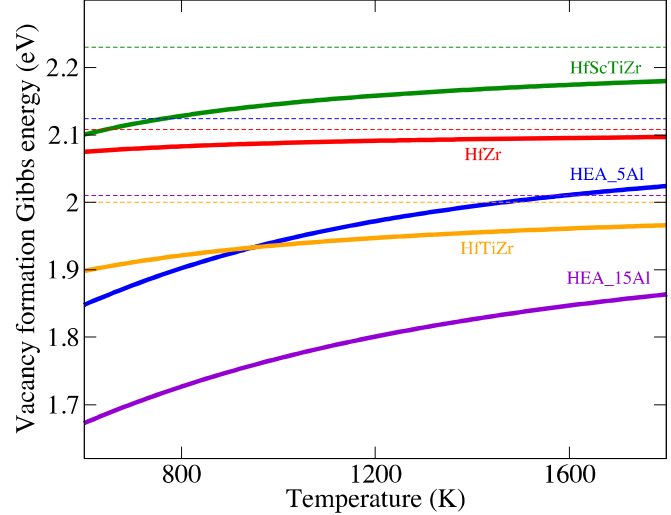


**Fig. 8.** Calculated temperature-dependent effective vacancy formation Gibbs energies for the investigated alloys. The horizontal dashed lines show the corresponding  $\bar{\epsilon}_v^f$  value for each alloy.

to the lowering of the magnitude of the excess configurational entropy which will be discussed in the following.

Fitting the total vacancy concentrations to an Arrhenius ansatz Eq. (10) yields the temperature-dependent effective vacancy formation Gibbs energy  $\tilde{G}_v^f(T)$ , as shown in Fig. 8. The corresponding temperature-dependent entropies of formation  $\tilde{S}_v^f(T)$  calculated via Eq. (11) are shown in Fig. 9. A general trend observed in Fig. 8 is an increase of the effective vacancy formation Gibbs energy  $\tilde{G}_v^f$  with increasing temperature, suggesting a negative effective vacancy formation entropy  $\tilde{S}_v^f$ , as demonstrated explicitly in Fig. 9. The negative  $\tilde{S}_v^f$  is a consequence of the multiple local vacancy neighborhoods. At low temperatures vacancies occur in the most favorable environments only, while at high temperatures less favorable environments provide vacancies as well. It turns out that contributions from different vacancy neighborhoods at low temperatures are well distinguishable while at very high temperatures all types of vacancies provide nearly equal contributions to the total concentration.

Consequently,  $\tilde{G}_v^f$  and  $\tilde{S}_v^f$  are both more sensitive to temperature at low temperatures than at high temperatures. To highlight this point, we define two temperature ranges,  $T_{\text{low}} = 600\text{--}1200$  K and  $T_{\text{high}} = 1200\text{--}1800$  K, and extract temperature-independent  $\tilde{S}_v^f$  and  $\tilde{H}_v^f$  according to Eqs. (12) and (13). The results are listed in Table 1. The magnitude of the  $\tilde{S}_v^f$  values for all the alloys is considerably larger at  $T_{\text{low}}$  than at  $T_{\text{high}}$  (at least by a factor of 2). Thus, in particular in the  $T_{\text{low}}$  temperature range, the  $\tilde{S}_v^f$  contribution cannot be neglected. For the binary HfZr, we obtain an  $\tilde{S}_v^f$  of  $-0.31$   $k_B$  at  $T_{\text{low}}$  which is comparable with the value of  $-0.4$   $k_B$  reported

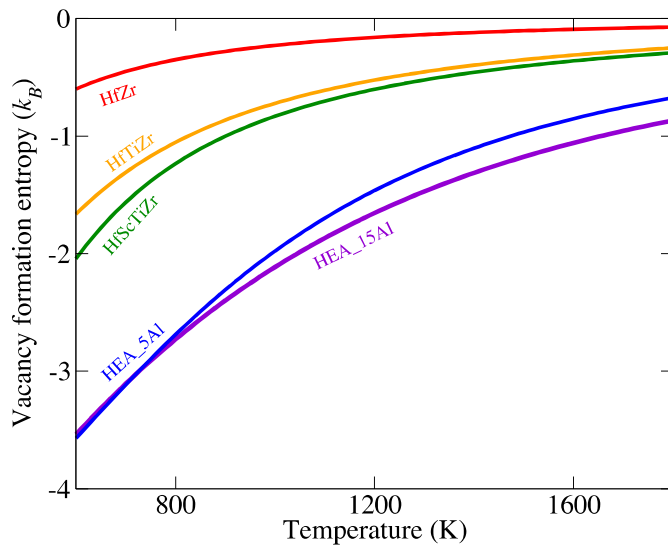


**Fig. 9.** Calculated temperature-dependent effective vacancy formation entropies for the investigated alloys.

for the binary CuNi at a 50-50 composition within a similar temperature range [17]. For the higher order systems, the  $\tilde{S}_v^f$  magnitudes are significant at both,  $T_{\text{low}}$  and  $T_{\text{high}}$ , with values in the order of  $-1 k_B$  and  $-2 k_B$ , with the lowest value even going down to  $-2.48 k_B$  (HEA\_15Al).

Note that the effective vacancy formation entropy only contains configurational excitations. Other thermal effects, e.g., vibrational or electronic excitations, tend to provide positive contributions to the entropy of vacancy formation, see e.g. Refs. [11,48]. As a consequence, we can expect a temperature-dependent competition between the configurational entropy and entropies from thermal excitations. At low temperatures a large negative configurational entropy may hardly be fully compensated by the weak thermal excitations, resulting in an increase of  $\tilde{G}_v^f$  with temperature. The vibrational entropy, however, may win at high temperatures as the configurational entropy becomes then very small. A maximal effective vacancy formation Gibbs energy may be expected at a certain intermediate temperature. As the high temperature limit is approached,  $\tilde{G}_v^f$  will converge to the mean value  $\bar{\epsilon}_v^f$  of the VF-DOS, as marked in Fig. 8 with the horizontal, dotted, colored lines. It is then evident that the mean value of the VF-DOS represents only the upper limit of  $\tilde{G}_v^f$ . The VF-DOS' for all investigated alloys show a considerable number of states with energies lower than the values predicted from Vegard's law, i.e., the states left to the dashed line in Fig. 5. The approximate  $E_v^{\text{reg}}$  values therefore generally overestimate the extrapolated  $\tilde{H}_v^f$  values (see Table 1). By adding the negative formation entropy at finite temperature, a better agreement with the resulting  $\tilde{G}_v^f$  can be achieved.

Excitations of specific local vacancy environments can be examined by the temperature-dependent concentration profiles of the vacancy neighborhood as obtained from Eq. (14) and shown in Fig. 10. In general we observe that the averaged local chemical environments favoring vacancy formation vary significantly with temperature. Especially at low temperatures, the concentrations of the most probable vacancy neighborhoods exhibit considerable deviations from the nominal alloy compositions. The origin of these deviations lies again in the fact that vacancies occur preferentially on the energetically most favorable positions instead of the positions that locally posses the overall alloy composition. This indicates that the widely-applied coherent potential approximation (CPA) method may not be accurate for vacancies in concentrated alloys if the composition of the alloy is used for the effective medium surrounding the vacancy. Instead, the concentration of the

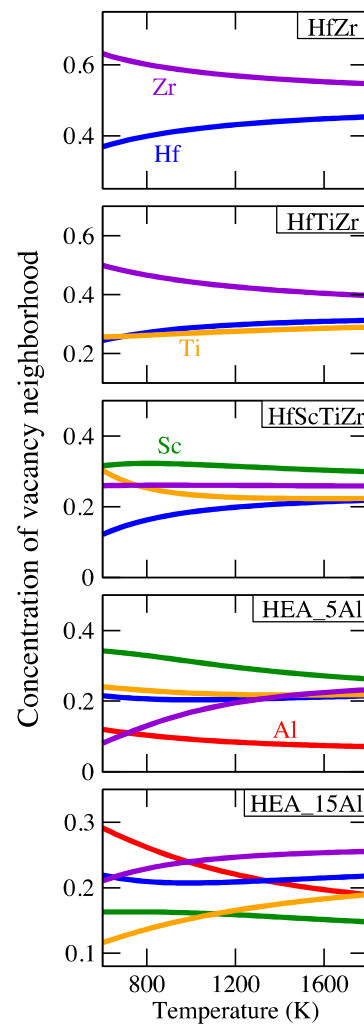


**Fig. 10.** Calculated temperature-dependent concentrations of the vacancy neighborhood, i.e., the 1st and 2nd shells around a vacancy.

vacancy neighborhood as calculated in the present work may provide more accurate references for the CPA vacancy energetics.

It should be noticed that the above thermodynamic analysis is based on the assumption that the alloys are random HCP solid solutions which may not hold for all investigated alloys in the considered temperature range. More specifically, the investigated HEAs are subject to an order-disorder transition at a critical temperature of about 1200 K [34] and for lower order systems the corresponding critical temperatures for an HCP to BCC transition are estimated as  $\sim 1500$  K [34] for HfZr and  $\sim 1200$  K [49] for HfTiZr. Therefore, the present calculated data apply only to the condition that the alloys remain homogeneous random solid solutions. The existence of short-range order (SRO) may have an impact on the VF-DOS through the variations of the alloy mixing behavior and chemical potentials. Once the VF-DOS for a structure with SRO is known, the current model can also be applied to predict finite-temperature vacancy properties for nonrandom alloys with SRO. The impact of SRO, however, cannot be generally described without explicit calculations or simulations, e.g., Monte Carlo simulations. Such an analysis requires a separate study.

#### 4.3. Vacancy migration KRA barriers

We have systematically investigated the impact of the alloy system, the migration direction, the migrating element, and vari-

ous local environments on vacancy migration barriers by means of DFT NEB calculations and the LCE technique. The results are shown in Fig. 11. Similarly as for the VF-DOS', the smooth VM-DOS' shown in Fig. 11 are the result of a Gaussian smearing using Eq. (21) with the same smearing parameter. As the NEB calculations are computationally demanding, we selected 15 random configurations for each element, migration direction, and alloy, resulting in  $(2 + 3 + 4 + 5 + 5) \times 2 \times 15 + 10 = 580$  (+10 for the pure metals) explicit NEB calculations. These extensive DFT NEB data provide a reasonable number of input structures for the LCE fitting. For each DFT VM-DOS in Fig. 11, the mean position is marked by a vertical line. Table 2 compiles the whole data set of the average vacancy migration energies calculated in this work.

Like for the VF-DOS', a wide distribution of the energy states contributing to the VM-DOS' can be observed for the higher order systems, i.e., from the ternary to the HEAs. A closer look on the energy scale reveals that the spread of the VM-DOS', i.e., the difference between the highest and lowest energies, can be larger than 1 eV while for the VF-DOS' it was mostly smaller than 1 eV, indicating that the migration of a vacancy is more sensitive to the local chemical environment than its formation. This is consistent with previous DFT calculations for the fcc NiFeMnCr system [29]. The large scatter of the migration barriers suggests a strongly correlated movement of the vacancy as it travels on the potential energy surface as was already shown in Ref. [23] based on a model CE study. Comparing the magnitude of the calculated barriers for the HCP HEAs of the present work with DFT NEB studies for other HEAs, e.g., the FCC Cantor alloy [30], we find that all of them roughly fall within a similar range of about 0.5 to 1.0 eV, regardless of the migrating species. Due to the variety of the local migration environments, the statistics of previous DFT NEB studies on HEAs [29,30] needs, however, to be reconsidered since the analysis was typically based on 4–6 NEB calculations per element. In the present work, the optimized LCEs further improve the limited sampling of the DFT VM-DOS' by additionally sampling 200 random migration configurations, yielding refined VM-DOS' for extended migration phase spaces (dashed DOS' in Fig. 11). As regards the “high entropy” effect, we do not observe any monotonic increase nor decrease of the mean KRA barriers with increasing number of components for any of the migrating species. A comparison among the columns in Table 2 reveals that Sc and Zr have relatively low (mean) KRA barriers while Al has the highest barriers to exchange with vacancies. Sc- and Zr-rich environments are energetically favorable to vacancies, see column 3 and 5 in Fig. 6. This strongly suggests that the movement of vacancies is highly correlated with the movement of Sc and Zr atoms, indicating that they are fast diffusors with high tracer diffusivities. The movement of the vacancy can also be accelerated by adding these elements. The increased tracer diffusion rates of Zr in HEA\_5Al with respect to that in pure Zr has already been reported in Ref. [35]. The increased phase stability with Al may be responsible for the high migration barriers. Thus in general, the preference of vacancies to be formed and to migrate in certain, element-specific environments indicates that composition-dependent diffusion rates may be achieved by tuning the composition of specific elements.

The data shown in Fig. 11 and Table 2 contain information on the anisotropy of vacancy migration. Colored VM-DOS' correspond to migration perpendicular to the HCP *c* axis, and the black ones to out-of-basal-plane migration. Although small differences can be seen in the shapes, the mean values of the  $E^{KRA}$  for the two migration directions are mostly similar with differences below 0.1 eV. Some exceptions are observed for Hf, Ti, and Zr with differences reaching up to 0.3 eV. A detailed analysis of the DFT NEB minimum energy pathways revealed that some migration paths for these elements within the basal plane show double saddle points as re-

ported for pure Ti in Ref. [50]. The middle point of these special migration pathways shows a significant displacement from the geometrical middle of the two endpoints, shifting towards the atom labelled with “2\*” in Fig. 3(b). Such a pathway with double saddle points occurs in all investigated alloys and metals. The occurrence of the double saddle points gets fewer as the number of components increases. This may be due to the strong repulsive interactions of the two closest atoms (labelled with 1) with the migrating atom in the middle of the pathway.

Note that Fig. 11 represents KRA barriers, i.e., the mean barriers of the forward and backward migration. The broadening of the *direction-dependent* barriers may become even more pronounced if the associated  $\delta$  is large, e.g.,  $> 0.1$  eV, as in the investigated HEAs. A large  $\delta$  indicates a severely asymmetrical vacancy-atom exchange frequency, e.g., for the energy profile in Fig. 2 it is much more likely to move to the left than to the right. The magnitude of  $\delta$  is closely related to the VF-DOS since the migration endpoints are positions where a single vacancy is located. From the values in the brackets in Table 2 one may find that  $\delta$  roughly increases with increasing number of components. Asymmetrical migration barriers, i.e., large  $\delta$  values were originally claimed to be the origin of the “sluggish diffusion” in HEAs [51]. However, a recent KMC study [52] showed that a wide distribution of the saddle point energies together with a narrow distribution of local energy minima can significantly enhance the mobility of the vacancy, suggesting that “non-sluggish” diffusion is possible as well. A common limitation of these arguments lies in the fact that in the corresponding studies the migration barriers and the local energy minima were assumed to be *randomly and independently* distributed. This is an unrealistic assumption because of short ranged correlations between the migration paths due to similar local chemical environments. In particular, geometrically nearby migration barriers and formation energies are likely to feature similar values.

#### 4.4. Potential energy surface of vacancy migration

An overall picture of the formation and migration of vacancies can be obtained by analyzing the potential energy surface (PES). To this end, we plot in Fig. 12 the PES of vacancy migration within one selected HCP basal plane for (a) the HfZr binary and (b) HEA\_15Al using the calculated vacancy formation and migration energetics. The black dots connected by dashed lines indicate the HCP lattice positions and the corresponding energy values refer to the formation energies of the respective atom being vacated. The saddle point of each individual migration path is projected to the geometric middle point marked by a gray cross for illustration. The saddle point energy is obtained from Eq. (15) where the  $E_v^{KRA}$  value is taken from the mean KRA migration barrier of two atoms at the endpoints. The actual *direction-dependent* migration barrier for each path is then simply the energy difference between the saddle point (gray cross) and one endpoint (black dot).

Fig. 12 reveals a clear difference between the PES for the HfZr binary and HEA\_15Al. For the HfZr binary, as may have been anticipated from the narrow broadening of the VF- and VM-DOS', vacancies travel on a smooth PES with regularly distributed valleys and peaks and only minor fluctuations in the energies. The *direction-dependent* migration barriers are almost symmetrical, i.e., the  $\delta$  values are small, as the vacancy formation energy is less sensitive to the local environment. The potential landscape for the HEA\_15Al alloy is, in contrast, significantly roughened [see Fig. 12(b)] as the local chemical environment critically influences the energetics. Compared to the binary, higher peaks and deeper valleys can be clearly observed, suggesting non-symmetrical individual migration pathways. It should be emphasized that these vacancy formation and migration energies are *not* randomly and independently

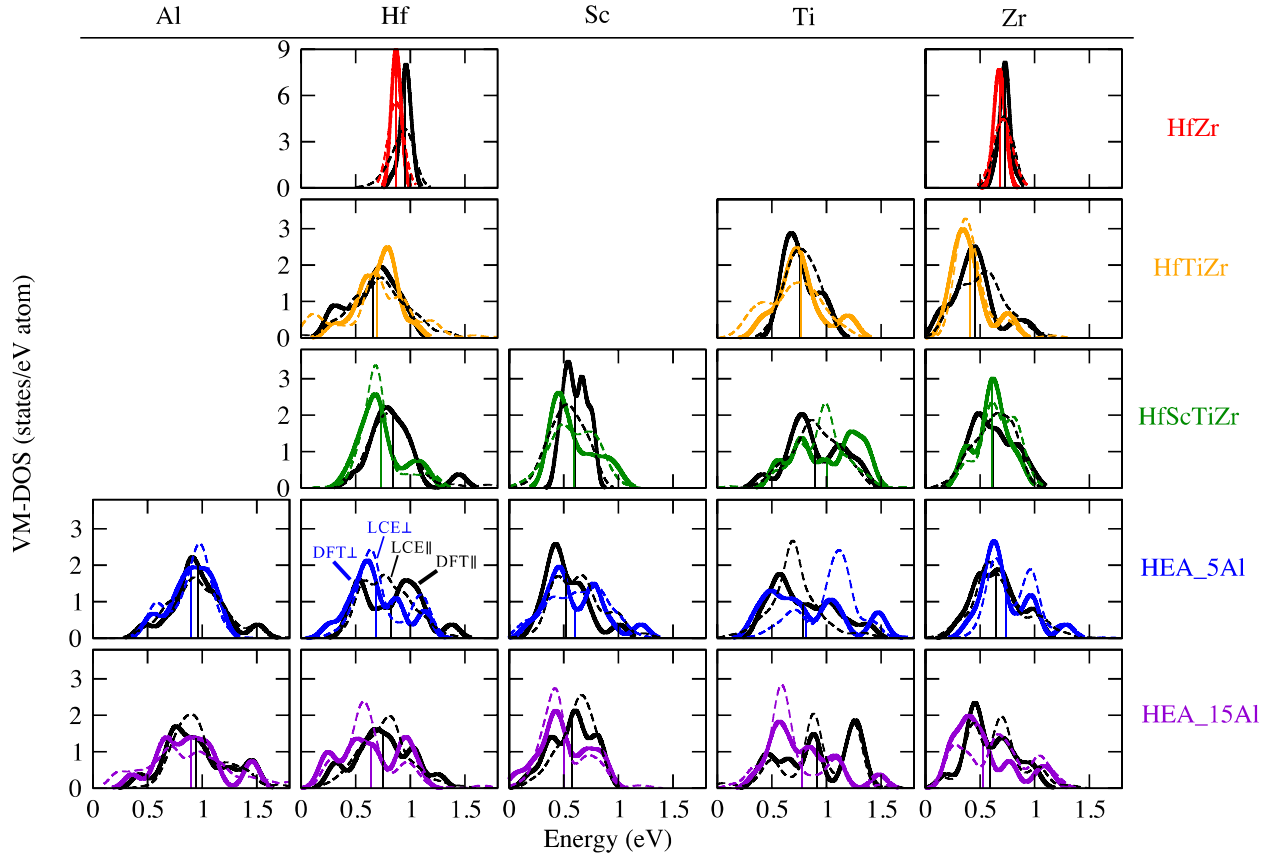


**Fig. 11.** Densities of vacancy migration states (VM-DOS) for all investigated alloys. Each column shows the VM-DOS for one type of alloying element. Solid, colored (black) DOS' show the DFT NEB results for the migration direction perpendicular (parallel) to the HCP  $c$  axis. Each DFT VM-DOS (solid curves) is obtained from 15 explicit NEB calculations. The dashed VM-DOS' are the results predicted by LCEs for 200 random local migration environments. (For interpretation of the references to colour in this figure legend, the reader is referred to the web version of this article.)

**Table 2**

Calculated vacancy migration KRA barriers (in unit of eV) for all investigated alloys. The migration direction “ $\perp$ ” (“ $\parallel$ ”) refers to the direction perpendicular (parallel) to the HCP  $c$  axis. Each DFT value is obtained by averaging over 15 KRA barriers and each LCE value is the average of 200 random migration configurations. For the DFT results, the average value of the  $\delta$  (eV) described in the main text is shown in each bracket.

| Alloy/Metal | Migration direction | Al         |      | Hf         |      | Sc         |      | Ti         |      | Zr         |      |
|-------------|---------------------|------------|------|------------|------|------------|------|------------|------|------------|------|
|             |                     | DFT        | LCE  |
| Pure metal  | $\perp$             | 0.48(0)    |      | 0.97(0)    |      | 0.66(0)    |      | 0.58(0)    |      | 0.60(0)    |      |
|             | $\parallel$         | 0.51(0)    |      | 1.01(0)    |      | 0.64(0)    |      | 0.57(0)    |      | 0.67(0)    |      |
| HfZr        | $\perp$             |            |      | 0.87(0.03) | 0.86 |            |      |            |      | 0.68(0.03) | 0.70 |
|             | $\parallel$         |            |      | 0.95(0.03) | 0.91 |            |      |            |      | 0.73(0.04) | 0.72 |
| HfTiZr      | $\perp$             |            |      | 0.70(0.05) | 0.70 |            |      |            |      | 0.76(0.05) | 0.69 |
|             | $\parallel$         |            |      | 0.66(0.06) | 0.71 |            |      |            |      | 0.76(0.05) | 0.77 |
| HfScTiZr    | $\perp$             |            |      | 0.73(0.05) | 0.72 | 0.59(0.04) | 0.59 | 1.01(0.07) | 0.94 | 0.61(0.09) | 0.67 |
|             | $\parallel$         |            |      | 0.84(0.05) | 0.85 | 0.61(0.06) | 0.53 | 0.90(0.07) | 0.90 | 0.62(0.08) | 0.62 |
| HEA_5Al     | $\perp$             | 0.90(0.11) | 0.89 | 0.69(0.09) | 0.75 | 0.60(0.11) | 0.62 | 0.81(0.10) | 1.03 | 0.73(0.09) | 0.82 |
|             | $\parallel$         | 0.96(0.08) | 0.97 | 0.83(0.13) | 0.78 | 0.52(0.12) | 0.64 | 0.79(0.08) | 0.71 | 0.65(0.08) | 0.67 |
| HEA_15Al    | $\perp$             | 0.90(0.09) | 0.90 | 0.64(0.09) | 0.62 | 0.50(0.15) | 0.50 | 0.78(0.12) | 0.68 | 0.53(0.10) | 0.64 |
|             | $\parallel$         | 0.95(0.12) | 0.99 | 0.75(0.12) | 0.76 | 0.57(0.13) | 0.61 | 0.92(0.12) | 0.92 | 0.59(0.11) | 0.63 |

distributed. For both the binary and HEA, regions with relatively rough and flat landscapes can be distinguished due to the similarity of the chemical environment within a certain region.

The individual migration paths on the potential energy surfaces shown in Fig. 12 can be categorized into four scenarios with different combinations of high and low  $E^{\text{KRA}}$  and  $\delta$  as shown in Fig. 13. While it was argued that the high  $\delta$  cases (right panel) may lead to thermodynamic vacancy (or atomic) trapping, the low  $\delta$  cases, especially together with a low  $E^{\text{KRA}}$  (left black path), may result

in a “kinetic trapping” of vacancies. In such a scenario, vacancies can easily migrate forward but also backward, i.e., oscillating locally without further movement, as shown in Fig. 3 of Ref. [23]. “Kinetic trapping” refers in particular to a situation where the location of the vacancy oscillations is not necessarily a lower energy position compared with the neighboring energy minima. The trapping effect is purely due to kinetics and it can significantly retard diffusion rates. As temperature increases, “kinetic trapping” may also occur for the low  $\delta$  and high  $E^{\text{KRA}}$  case (left red path). For

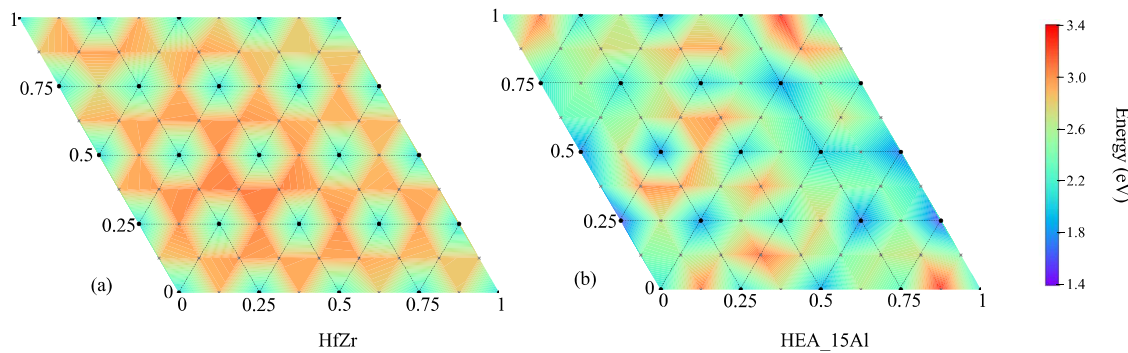


**Fig. 12.** Potential energy surfaces of vacancy migration on a selected HCP basal plane of the corresponding SQS supercell for (a) the binary HfZr alloy and (b) the HEA\_15Al alloy. Fractional coordinates are used.

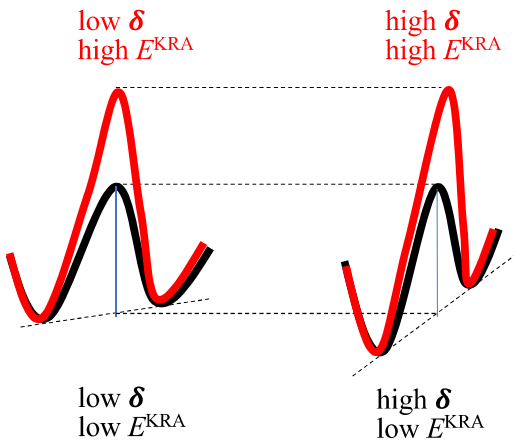


**Fig. 13.** Illustration of four different scenarios for a local vacancy migration path resulting from low and high KRA barriers and low and high  $\delta$  values.

the same height of the  $E^{KRA}$ , the vacancy oscillations may become less probable with increasing  $\delta$  because the backward movement becomes more difficult, cf. the left and right paths in Fig. 13. As vacancies frequently migrate along the most favorable pathways, at low temperatures, if the individual paths of significantly low  $E^{KRA}$  with high  $\delta$  are locally well-connected in the alloys, the movement of vacancies can be significantly accelerated. This analysis highlights the importance of taking the correlation of  $E^{KRA}$  and  $\delta$  into account when simulating diffusion processes in HEAs.

## 5. Conclusions

Vacancy formation and migration energies and derived properties for HCP Al-Hf-Sc-Ti-Zr HEAs including related subsystems have been comprehensively investigated by *ab initio* DFT simulations. The environment-dependent vacancy formation energy density-of-states (VF-DOS) and chemical potentials have been computed for the chemically disordered phases by sampling SQS supercells. The chemical potentials show deviations from the pure metals of less than  $\pm 0.1$  eV except for Al ( $-0.7$  eV) suggesting a significant enhancement of the phase stability due to Al. The VF-DOS exhibit a significant broadening ( $> 0.6$  eV) for higher order systems with mean values deviating strongly from the predictions of Vegard's law. Only the HfZr binary is an exception and closely follows Vegard's law. The broadening increases with increasing the number of elements, indicating a "high entropy" effect. Analysis of the vacancy neighborhoods shows that Sc-, Zr-, and Al-rich environments are favorable for vacancies and Hf- and Ti-rich environments are unfavorable.

Vacancy concentrations at finite temperatures have been extracted from a statistical analysis based upon a well-defined formula for the configurational entropy. A clear deviation from Arrhenius' linear dependence has been revealed. A systematic dependence on the number of elements ("high entropy" effect) could not be found. At low temperatures, the vacancy concentrations of the different alloys differ by 4 orders of magnitude, while at high temperatures the differences become smaller. The effective vacancy formation Gibbs energies increase strongly with temperature for the higher order systems due to a large negative configurational formation entropy. The latter originates in the broadening of the VF-DOS' and is thus a consequence of the strong impact of the local chemical environment on vacancy formation. Neither the mean value of the VF-DOS' nor Vegard's law can therefore provide accurate predictions. The temperature-dependent concentrations of the vacancy neighborhoods severely deviate from the alloys' compositions. This suggests that the accuracy of CPA calculations for vacancies needs to be improved.

A total number of 580 DFT NEB calculations has been performed to sample the vacancy migration energy density-of-states (VM-DOS). Extended vacancy migration phase spaces have been further sampled by applying the local cluster expansion technique. The VM-DOS' exhibit wide distributions ( $> 1$  eV) larger than the VF-DOS' suggesting that migration barriers are more sensitive to the chemical environment. There is no obvious indication of the "high entropy" effect. On average, Sc and Zr have low barriers while Al has the highest. Sc and Zr are thus predicted to be fast diffusers, which further suggests that diffusion rates may be sensitive to the content of these elements. A pronounced anisotropy in the VM-DOS' is not observed for any of the alloys. However, within the HCP basal plane, a large number of migration pathways with double saddle points has been observed for the group IV elements Hf, Ti, and Zr, similarly as reported for pure Ti.

Based on the extensive data set of vacancy formation and migration energies critical insights into the migration mechanisms could be derived. The wide distributions of the VF-DOS' can enhance individual, asymmetric vacancy-atom exchanges, which points toward the presence of "thermodynamic traps" for vacancies. Our results indicate that the asymmetry (i.e., the  $\delta$  in the KRA barrier definition) increases with the number of components. On the other hand, the asymmetric migration environments may reduce the possibility of "kinetic traps" for vacancies. As vacancies frequently migrate along the most favorable pathways at low temperatures, the movement of vacancies can be significantly accelerated if asymmetric paths with low KRA barriers are well connected. "Sluggish diffusion" is not seen to be a general core effect for HEAs.

## Data Availability

The authors declare that all data supporting the findings of this study are available from the corresponding author on reasonable request.

## Declaration of Competing Interest

The authors declare that they have no known competing financial interests or personal relationships that could have appeared to influence the work reported in this paper.

## Acknowledgments

XZ thanks Professor Marcel H.F. Sluiter for fruitful discussions. The authors thank Dr. Mayur Vaidya and Mr. Hemanth Kumar Sandireddy (IIT Hyderabad, India) for the help with the thermodynamic calculations. Financial support from the Deutsche Forschungsgemeinschaft (DFG) via the research projects DI 1419/17-1 and GR 3716/5-1 is gratefully acknowledged. The authors also acknowledge support by the state of Baden-Württemberg through bwHPC and the DFG through grant no INST 40/467-1 FUGG (JUSTUS cluster) and the support by the Stuttgart Center for Simulation Science (SimTech).

## Supplementary material

Supplementary material associated with this article can be found, in the online version, at doi:[10.1016/j.actamat.2022.117677](https://doi.org/10.1016/j.actamat.2022.117677).

## References

- [1] M. Vaidya, S. Trubel, B. Murty, G. Wilde, S. Divinski, Ni tracer diffusion in CoCr-FeNi and CoCrFeMnNi high entropy alloys, *Journal of Alloys and Compounds* 688 (2016) 994–1001, doi:[10.1016/j.jallcom.2016.07.239](https://doi.org/10.1016/j.jallcom.2016.07.239).
- [2] M. Zajusz, J. Dąbrowska, M. Danielewski, Determination of the intrinsic diffusivities from the diffusion couple experiment in multicomponent systems, *Scripta Materialia* 138 (2017) 48–51, doi:[10.1016/j.scriptamat.2017.05.031](https://doi.org/10.1016/j.scriptamat.2017.05.031).
- [3] M. Vaidya, K. Pradeep, B. Murty, G. Wilde, S. Divinski, Bulk tracer diffusion in CoCrFeNi and CoCrFeMnNi high entropy alloys, *Acta Materialia* 146 (2018) 211–224, doi:[10.1016/j.actamat.2017.12.052](https://doi.org/10.1016/j.actamat.2017.12.052).
- [4] J.-W. Yeh, Recent progress in high-entropy alloys, *European Journal of Control* 31 (2006) 633–648, doi:[10.3166/acsm.31.633-648](https://doi.org/10.3166/acsm.31.633-648).
- [5] S.V. Divinski, A.V. Pokrov, N. Esakkiraja, A. Paul, A mystery of “sluggish diffusion” in high-entropy alloys: The truth or a myth? *Diffusion Foundations* 17 (2018) 69–104, doi:[10.4028/www.scientific.net/DF.17.69](https://doi.org/10.4028/www.scientific.net/DF.17.69).
- [6] D. Gaertner, J. Kottke, Y. Chumlyakov, F. Hergemiller, G. Wilde, S.V. Divinski, Tracer diffusion in single crystalline CoCrFeNi and CoCrFeMnNi high-entropy alloys: Kinetic hints towards a low-temperature phase instability of the solid-solution? *Scripta Materialia* 187 (2020) 57–62, doi:[10.1016/j.scriptamat.2020.05.060](https://doi.org/10.1016/j.scriptamat.2020.05.060).
- [7] E.-W. Huang, H.-S. Chou, K.N. Tu, W.-S. Hung, T.-N. Lam, C.-W. Tsai, C.-Y. Chang, B.-H. Lin, A.-C. Yeh, S.-H. Chang, Y.-J. Chang, J.-J. Yang, X.-Y. Li, C.-S. Ku, K. An, Y.-W. Chang, Y.-L. Jao, Element effects on high-entropy alloy vacancy and heterogeneous lattice distortion subjected to quasi-equilibrium heating, *Scientific Reports* 9 (1) (2019) 14788, doi:[10.1038/s41598-019-51297-4](https://doi.org/10.1038/s41598-019-51297-4).
- [8] K. Sugita, N. Matsuoaka, M. Mizuno, H. Araki, Vacancy formation enthalpy in CoCrFeMnNi high-entropy alloy, *Scripta Materialia* 176 (2020) 32–35, doi:[10.1016/j.scriptamat.2019.09.033](https://doi.org/10.1016/j.scriptamat.2019.09.033).
- [9] L. Resch, M. Luckabauer, N. Helthuis, N.L. Okamoto, T. Ichitsubo, R. Enzinger, W. Sprengel, R. Würschum, Search for vacancies in concentrated solid-solution alloys with fcc crystal structure, *Phys. Rev. Materials* 4 (2020) 060601, doi:[10.1103/PhysRevMaterials.4.060601](https://doi.org/10.1103/PhysRevMaterials.4.060601).
- [10] D.E. Jodi, T.A. Listyawan, P. Hruska, J. Cizek, N. Park, U. Lee, Study of vacancies in Fe<sub>x</sub>(CoCrMnNi)<sub>100-x</sub> medium- and high-entropy alloys by positron annihilation spectroscopy, *Scripta Materialia* 194 (2021) 113654, doi:[10.1016/j.scriptamat.2020.113654](https://doi.org/10.1016/j.scriptamat.2020.113654).
- [11] A. Glensk, B. Grabowski, T. Hickel, J. Neugebauer, Breakdown of the Arrhenius Law in Describing Vacancy Formation Energies: The Importance of Local Anharmonicity Revealed by Ab initio Thermodynamics, *Phys. Rev. X* 4 (2014) 011018, doi:[10.1103/PhysRevX.4.011018](https://doi.org/10.1103/PhysRevX.4.011018).
- [12] X. Zhang, B. Grabowski, T. Hickel, J. Neugebauer, Calculating free energies of point defects from ab initio, *Computational Materials Science* 148 (2018) 249–259, doi:[10.1016/j.commatsci.2018.02.042](https://doi.org/10.1016/j.commatsci.2018.02.042).
- [13] X. Zhang, B. Grabowski, F. Körmann, A.V. Ruban, Y. Gong, R.C. Reed, T. Hickel, J. Neugebauer, Temperature dependence of the stacking-fault Gibbs energy for Al, Cu, and Ni, *Phys. Rev. B* 98 (2018) 224106, doi:[10.1103/PhysRevB.98.224106](https://doi.org/10.1103/PhysRevB.98.224106).
- [14] A. Forslund, X. Zhang, B. Grabowski, A.V. Shapeev, A.V. Ruban, *Ab initio* simulations of the surface free energy of TiN(001), *Phys. Rev. B* 103 (2021) 195428, doi:[10.1103/PhysRevB.103.195428](https://doi.org/10.1103/PhysRevB.103.195428).
- [15] A. Van der Ven, G. Ceder, Vacancies in ordered and disordered binary alloys treated with the cluster expansion, *Phys. Rev. B* 71 (2005) 054102, doi:[10.1103/PhysRevB.71.054102](https://doi.org/10.1103/PhysRevB.71.054102).
- [16] J.B. Piochaud, T.P.C. Klaver, G. Adjanor, P. Olsson, C. Domain, C.S. Becquart, First-principles study of point defects in a fcc Fe-10Ni-20Cr model alloy, *Phys. Rev. B* 89 (2014) 024101, doi:[10.1103/PhysRevB.89.024101](https://doi.org/10.1103/PhysRevB.89.024101).
- [17] X. Zhang, M.H.F. Sluiter, *Ab initio* prediction of vacancy properties in concentrated alloys: The case of fcc Cu-Ni, *Phys. Rev. B* 91 (2015) 174107, doi:[10.1103/PhysRevB.91.174107](https://doi.org/10.1103/PhysRevB.91.174107).
- [18] S. Zhao, G.M. Stocks, Y. Zhang, Defect energetics of concentrated solid-solution alloys from ab initio calculations: Ni<sub>0.5</sub>Co<sub>0.5</sub>, Ni<sub>0.5</sub>Fe<sub>0.5</sub>, Ni<sub>0.8</sub>Fe<sub>0.2</sub> and Ni<sub>0.8</sub>Cr<sub>0.2</sub>, *Phys. Chem. Chem. Phys.* 18 (2016) 24043–24056, doi:[10.1039/C6CP05161H](https://doi.org/10.1039/C6CP05161H).
- [19] A. Manzoor, Y. Zhang, D.S. Aidhy, Factors affecting the vacancy formation energy in Fe<sub>70</sub>Ni<sub>10</sub>Cr<sub>20</sub> random concentrated alloy, *Computational Materials Science* 198 (2021) 110669, doi:[10.1016/j.commatsci.2021.110669](https://doi.org/10.1016/j.commatsci.2021.110669).
- [20] A. Van der Ven, G. Ceder, M. Asta, P. Tepeš, First-principles theory of ionic diffusion with nondilute carriers, *Physical Review B* 64 (18) (2001) 184307, doi:[10.1103/PhysRevB.64.184307](https://doi.org/10.1103/PhysRevB.64.184307).
- [21] A. Van der Ven, G. Ceder, First principles calculation of the interdiffusion coefficient in binary alloys, *Physical Review Letters* 94 (4) (2005) 045901, doi:[10.1103/PhysRevLett.94.045901](https://doi.org/10.1103/PhysRevLett.94.045901).
- [22] X. Zhang, M.H.F. Sluiter, Cluster expansions for thermodynamics and kinetics of multicomponent alloys, *Journal of Phase Equilibria and Diffusion* 37 (1) (2016) 44–52, doi:[10.1007/s11069-015-0427-x](https://doi.org/10.1007/s11069-015-0427-x).
- [23] X. Zhang, M.H.F. Sluiter, Kinetically driven ordering in phase separating alloys, *Phys. Rev. Materials* 3 (2019) 095601, doi:[10.1103/PhysRevMaterials.3.095601](https://doi.org/10.1103/PhysRevMaterials.3.095601).
- [24] A.V. Ruban, Thermal vacancies in random alloys in the single-site mean-field approximation, *Phys. Rev. B* 93 (2016) 134115, doi:[10.1103/PhysRevB.93.134115](https://doi.org/10.1103/PhysRevB.93.134115).
- [25] S. Middleburgh, D. King, G. Lumpkin, M. Cortie, L. Edwards, Segregation and migration of species in the CrCoFeNi high entropy alloy, *Journal of Alloys and Compounds* 599 (2014) 179–182, doi:[10.1016/j.jallcom.2014.01.135](https://doi.org/10.1016/j.jallcom.2014.01.135).
- [26] W.-M. Choi, Y.H. Jo, S.S. Sohn, S. Lee, B.-J. Lee, Understanding the physical metallurgy of the CoCrFeMnNi high-entropy alloy: an atomistic simulation study, *npj Computational Materials* 4 (1) (2018) 1, doi:[10.1038/s41524-017-0060-9](https://doi.org/10.1038/s41524-017-0060-9).
- [27] W. Chen, X. Ding, Y. Feng, X. Liu, K. Liu, Z. Lu, D. Li, Y. Li, C. Liu, X.-Q. Chen, Vacancy formation enthalpies of high-entropy FeCoCrNi alloy via first-principles calculations and possible implications to its superior radiation tolerance, *Journal of Materials Science and Technology* 34 (2) (2018) 355–364, doi:[10.1016/j.jmst.2017.11.005](https://doi.org/10.1016/j.jmst.2017.11.005).
- [28] S. Zhao, T. Egami, G.M. Stocks, Y. Zhang, Effect of d electrons on defect properties in equiatomic NiCoCr and NiCoFeCr concentrated solid solution alloys, *Phys. Rev. Materials* 2 (2018) 013602, doi:[10.1103/PhysRevMaterials.2.013602](https://doi.org/10.1103/PhysRevMaterials.2.013602).
- [29] C. Li, J. Yin, K. Odbadrakh, B.C. Sales, S.J. Zinkle, G.M. Stocks, B.D. Wirth, First principle study of magnetism and vacancy energetics in a near equimolar NiFeMnCr high entropy alloy, *Journal of Applied Physics* 125 (15) (2019) 155103, doi:[10.1063/1.5086172](https://doi.org/10.1063/1.5086172).
- [30] M. Mizuno, K. Sugita, H. Araki, Defect energetics for diffusion in CrMnFeCoNi high-entropy alloy from first-principles calculations, *Computational Materials Science* 170 (2019) 109163, doi:[10.1016/j.commatsci.2019.109163](https://doi.org/10.1016/j.commatsci.2019.109163).
- [31] H. Guan, S. Huang, J. Ding, F. Tian, Q. Xu, J. Zhao, Chemical environment and magnetic moment effects on point defect formations in CoCrNi-based concentrated solid-solution alloys, *Acta Materialia* 187 (2020) 122–134, doi:[10.1016/j.actamat.2020.01.044](https://doi.org/10.1016/j.actamat.2020.01.044).
- [32] S. Zhao, Defect properties in a VTaCrW equiatomic high entropy alloy (HEA) with the body centered cubic (bcc) structure, *Journal of Materials Science and Technology* 44 (2020) 133–139, doi:[10.1016/j.jmst.2019.10.025](https://doi.org/10.1016/j.jmst.2019.10.025).
- [33] S.E. Daigle, D.W. Brenner, Statistical approach to obtaining vacancy formation energies in high-entropy crystals from first principles calculations: Application to a high-entropy diboride, *Phys. Rev. Materials* 4 (2020) 123602, doi:[10.1103/PhysRevMaterials.4.123602](https://doi.org/10.1103/PhysRevMaterials.4.123602).
- [34] L. Rogal, P. Bobrowski, F. Körmann, S. Divinski, F. Stein, B. Grabowski, Computationally-driven engineering of sublattice ordering in a hexagonal Al-Hf-Si-Ti-Zr high entropy alloy, *Scientific Reports* 7 (1) (2017) 2209, doi:[10.1038/s41598-017-02385-w](https://doi.org/10.1038/s41598-017-02385-w).
- [35] M. Vaidya, S. Sen, X. Zhang, L. Frommeyer, L. Rogal, S. Sankaran, B. Grabowski, G. Wilde, S.V. Divinski, Phenomenon of ultra-fast tracer diffusion of Co in HCP high entropy alloys, *Acta Materialia* 196 (2020) 220–230, doi:[10.1016/j.actamat.2020.06.025](https://doi.org/10.1016/j.actamat.2020.06.025).
- [36] D. Morgan, Y. Zhang, Comment on “thermal vacancies in random alloys in the single-site mean-field approximation”, *Phys. Rev. B* 101 (2020) 136101, doi:[10.1103/PhysRevB.101.136101](https://doi.org/10.1103/PhysRevB.101.136101).
- [37] A. Zunger, S.-H. Wei, L.G. Ferreira, J.E. Bernard, Special quasirandom structures, *Phys. Rev. Lett.* 65 (1990) 353–356, doi:[10.1103/PhysRevLett.65.353](https://doi.org/10.1103/PhysRevLett.65.353).
- [38] P.E. Blöchl, Projector augmented-wave method, *Phys. Rev. B* 50 (1994) 17953–17979, doi:[10.1103/PhysRevB.50.17953](https://doi.org/10.1103/PhysRevB.50.17953).
- [39] G. Kresse, J. Furthmüller, Efficient iterative schemes for ab initio total-energy calculations using a plane-wave basis set, *Phys. Rev. B* 54 (1996) 11169–11186, doi:[10.1103/PhysRevB.54.11169](https://doi.org/10.1103/PhysRevB.54.11169).
- [40] G. Kresse, J. Furthmüller, Efficiency of ab-initio total energy calculations for metals and semiconductors using a plane-wave basis set, *Computational Materials Science* 6 (1) (1996) 15–50, doi:[10.1016/0927-0256\(96\)00008-0](https://doi.org/10.1016/0927-0256(96)00008-0).

- [41] J.P. Perdew, K. Burke, M. Ernzerhof, Generalized gradient approximation made simple, *Phys. Rev. Lett.* 77 (1996) 3865–3868, doi:[10.1103/PhysRevLett.77.3865](https://doi.org/10.1103/PhysRevLett.77.3865).
- [42] M. Methfessel, A.T. Paxton, High-precision sampling for brillouin-zone integration in metals, *Phys. Rev. B* 40 (1989) 3616–3621, doi:[10.1103/PhysRevB.40.3616](https://doi.org/10.1103/PhysRevB.40.3616).
- [43] H.J. Monkhorst, J.D. Pack, Special points for brillouin-zone integrations, *Phys. Rev. B* 13 (1976) 5188–5192, doi:[10.1103/PhysRevB.13.5188](https://doi.org/10.1103/PhysRevB.13.5188).
- [44] B. Widom, Some topics in the theory of fluids, *The Journal of Chemical Physics* 39 (11) (1963) 2808–2812, doi:[10.1063/1.1734110](https://doi.org/10.1063/1.1734110).
- [45] G. Henkelman, B.P. Uberuaga, H. Jnsson, A climbing image nudged elastic band method for finding saddle points and minimum energy paths, *The Journal of Chemical Physics* 113 (22) (2000) 9901–9904, doi:[10.1063/1.1329672](https://doi.org/10.1063/1.1329672).
- [46] G. Henkelman, H. Jnsson, Improved tangent estimate in the nudged elastic band method for finding minimum energy paths and saddle points, *The Journal of Chemical Physics* 113 (22) (2000) 9978–9985, doi:[10.1063/1.1323224](https://doi.org/10.1063/1.1323224).
- [47] A.R. Natarajan, P. Dolin, A. Van der Ven, Crystallography, thermodynamics and phase transitions in refractory binary alloys, *Acta Materialia* 200 (2020) 171–186, doi:[10.1016/j.actamat.2020.08.034](https://doi.org/10.1016/j.actamat.2020.08.034).
- [48] B. Grabowski, T. Hickel, J. Neugebauer, Formation energies of point defects at finite temperatures, *Physica status solidi (b)* 248 (6) (2011) 1295–1308, doi:[10.1002/pssb.201046302](https://doi.org/10.1002/pssb.201046302).
- [49] L. Lin, L. Delaey, O. Van Der Biest, P. Wollants, Calculation of isothermal sections of three ternary Ti-Zr-X systems, *Scripta Materialia* 34 (9) (1996) 1411–1416, doi:[10.1016/1359-6462\(96\)00006-1](https://doi.org/10.1016/1359-6462(96)00006-1).
- [50] S.L. Shang, L.G. Hector, Y. Wang, Z.K. Liu, Anomalous energy pathway of vacancy migration and self-diffusion in hcp Ti, *Phys. Rev. B* 83 (2011) 224104, doi:[10.1103/PhysRevB.83.224104](https://doi.org/10.1103/PhysRevB.83.224104).
- [51] K.-Y. Tsai, M.-H. Tsai, J.-W. Yeh, Sluggish diffusion in CoCrFeMnNi high-entropy alloys, *Acta Materialia* 61 (13) (2013) 4887–4897, doi:[10.1016/j.actamat.2013.04.058](https://doi.org/10.1016/j.actamat.2013.04.058).
- [52] S.I. Thomas, S. Patala, Vacancy diffusion in multi-principal element alloys: The role of chemical disorder in the ordered lattice, *Acta Materialia* 196 (2020) 144–153, doi:[10.1016/j.actamat.2020.06.022](https://doi.org/10.1016/j.actamat.2020.06.022).